Volume 16, Issue 2, 162503 (1-17)

International Journal of Industrial Chemistry (IJIC)

https://doi.org/10.57647/j.ijic.2025.1603.13

# Study of CO Hydrogenation over Cobalt-based Catalysts: Synergistic Effect

Arefeh Sadeghi Nikou[1] , Shahram Moradi Dehaghi[1,*], Yahya Zamani[1,2], Jafar Sadeghzadeh Ahari[1,2]

[1]*Department of Chemistry, NT.C., Islamic Azad University, Tehran, Iran*
[2]*Gas Research Division, Research Institute of Petroleum Industry, Tehran, Iran*

[*]**Corresponding author:** shm_moradi@iau.ac.ir

**Research Article**

Received:
6 February 2025

Revised:
2 June 2025

Accepted:
19 June 2025

Published in Issue:
30 June 2025



**Abstract:**

A series of cobalt-based catalysts were prepared using $\gamma$-$Al_2O_3$ as a support and cerium/zirconium mixed oxides as promoters, with varying Ce/Zr molar ratios. The 15Co/$\gamma$-$Al_2O_3$, 15Co/3Zr/$\gamma$-$Al_2O_3$, 15Co/3Ce/$\gamma$-$Al_2O_3$ and 15Co/1.5Zr/1.5Ce/$\gamma$-$Al_2O_3$ were synthesized using the wet impregnation method. BET, TGA, FE-SEM, XRD, $H_2$-TPR, and ICP techniques were used to determine the characteristics of the prepared catalysts. The findings showed that the catalyst (15Co/1.5Zr/1.5Ce/$\gamma$-$Al_2O_3$) with double promotion exceeded the performance of other catalysts, indicating notable synergistic effects. These effects are expected to play a crucial role in reducing side reactions that affect selectivity towards higher hydrocarbons. The 15Co/1.5Zr/1.5Ce/$\gamma$-$Al_2O_3$ catalyst demonstrated enhanced stability and reduced degradation during prolonged operation, resulting in higher CO conversion and effective suppression of excessive carbon chain growth. All prepared catalysts were tested in a fixed-bed reactor under a pressure of 27 bar, a temperature of 220 °C, and an $H_2$/CO ratio of 2. The results showed that the doubly-promoted catalyst achieved superior performance, with CO conversion, $C_5^+$ selectivity, and yield reaching 50.4 ± 1.5%, 82.3 ± 0.9%, and 41.5 ± 0.8%, respectively, compared to the other catalysts. In conclusion, these findings confirm the substantial influence of Zr and Ce promoters on the performance of Co-based catalysts during the Fischer-Tropsch synthesis reaction.

**Keywords:** CO hydrogenation, Cobalt catalyst, Fischer-Tropsch synthesis, Metal promoters, Synergistic effect

**Cite this article:** Sadeghi Nikou, A., Moradi Dehaghi, S., Zamani, Y., Jafar Sadeghzadeh, A. (2025). Study of CO Hydrogenation over Cobalt-based Catalysts: Synergistic Effect, *International Journal of Industrial Chemistry*, 16(3). https://doi.org/10.57647/j.ijic.2025.1603.13

## 1. Introduction

Fossil fuel resources are rapidly diminishing due to current levels of consumption [1]. There is growing interest in Fischer-Tropsch Synthesis (FTS), a process that converts syngas—a mixture of hydrogen and carbon monoxide sourced from natural gas, coal, and biomass—into liquid hydrocarbon fuels [2, 3]. FTS is a catalytic process that produces clean liquid fuels from syngas [4-6]. Also, FTS can be described as a polymerization process, wherein carbon-carbon bonds are created between carbon atoms originating from carbon monoxide, facilitated by hydrogen and a metal catalyst, with water produced as a byproduct [7, 8]. The fuels produced by the FTS process are of high quality, characterized by low aromatic content and the absence of sulfur [9]. From both economic and environmental perspectives, converting natural gas into liquid hydrocarbons (Gas-To-Liquids (GTL)) is a viable strategy in the energy sector [10-12]. The synthesis gas employed in this technique consists of carbon monoxide and hydrogen, with specific ratios varying depending on the method and source of the gas [13, 14].

The activity and selectivity of CO hydrogenation catalysts in FTS are significantly influenced by critical parameters such as metal loading, preparation process, support type, and the use of promoters [15-18]. The metals in "group eight" show higher reactivity in carbon-carbon coupling reactions. Iron [19], ruthenium [20-22], cobalt [23-28], and nickel are more active than manganese and are considered the best alternatives for the FTS reaction. Certain transition metals, particularly Co, Fe, and Ru, have shown significant catalytic activity in the FTS process [29, 30]. Promoted cobalt catalysts are preferred for long-chain hydrocarbons derived from natural gas. However, cobalt catalysts are mainly used to produce straight-chain hydrocarbons [31]. γ-Alumina is commonly used as a support for Co catalysts due to its favorable mechanical properties.

Cobalt-based catalysts offer several advantages over iron-based systems, including higher activity per unit mass of metal, enhanced resistance to deactivation by water, lower activity for the competing Water-Gas Shift (WGS) reaction, and reduced formation of oxygenated byproducts [32]. However, the high cost and limited availability of ruthenium-based catalysts present significant challenges for their commercial application [32, 33]. As a result, researchers have investigated a range of heterogeneous catalysts, both supported and unsupported, such as Fe and Co catalysts promoted with Pt, Ru, Ir, Re, Ag, K, Cu, and Pd [34-39]. Additionally, researchers continue to pursue in-depth studies in this area, aiming to achieve higher and more stable syngas conversions in the FTS process. While Ru, Fe, and Co remain the most active metals for FTS, the considerable cost disparity poses a significant challenge, as Ru is approximately 225 times more expensive than Co [40-42]. The choice between Co and Fe is mainly determined by the quality of the syngas utilized, particularly when the syngas is produced from natural gas or methane, resulting in $H_2/CO$ ratios greater than 2.0 (> 2.0) [43]. However, the cobalt catalyst is preferred due to its higher selectivity for hydrocarbons, lower WGS activity, and slower deactivation rates compared to the iron catalyst. Conversely, the Fe catalyst exhibits higher activity in the water-gas shift reaction, making it the preferred option for syngas obtained from coal or biomass with $H_2/CO$ ratios below 2.0 [44-46].

Various researchers have achieved high α values ranging from 0.9 to 0.95 through higher potassium loadings. Janani et al. [47] examined the effectiveness of mixed metal catalysts composed of Co and Ce for the FTS of aliphatic hydrocarbons. Their results showed that the carbonyl-based catalyst exhibited higher olefin selectivity (19–25%) and produced less methane (14%) compared to the dipicolinate catalyst (olefin selectivity: 15–16%, methane: 20%). Jacobs et al. [48] investigated $Co/Al_2O_3$ catalysts promoted with varying amounts of Group 11 metals (Cu, Ag, Au), characterized them, and tested them in a FTS reaction. Their findings revealed that small amounts of such metals enhanced Co reducibility and improved the surface Co metal active site densities in the cases of Ag and Au.

Moreover, alkali promoters significantly influence both the structure and catalytic performance of the catalyst. For instance, the alkali metals K, Rb, and Cs were more effective than Li and Na in facilitating shifts in the product distribution towards heavier hydrocarbons and olefins [49]. According to previous findings, potassium is commonly used as a promoter, with several advantages, including its lower cost compared to other Group I alkalis [50]. Potassium has been demonstrated to improve CO adsorption while reducing $H_2$ adsorption [51].

According to Khodakov's [52] findings, cobalt-supported catalysts are the optimal choice for producing long-chained hydrocarbons from syngas with a high $H_2/CO$ ratio. His research identified the impact of several factors, such as the composition of cobalt phases, the size of cobalt particles, the texture of the catalyst support, the variety of support materials, and the presence of noble metals, on the rates of FTS reactions, the selectivity of hydrocarbon production, and the stability of the catalyst. Furthermore, he investigated potential catalyst deactivation processes and the alteration of cobalt active sites during the reaction. The study also examined the impact of catalyst synthesis, using either hydrogen or carbon monoxide pretreatment, on the activity and selectivity of a cobalt-based ZnO catalyst (10 wt%-Co/ZnO) during the FTS reaction in a fixed-bed reactor. Their results demonstrated that hydrogen-pretreated cobalt surfaces showed higher activity, leading to greater methane and olefin selectivity compared to carbon monoxide-pretreated catalysts [53]. Cobalt-based FTS catalysts are crucial to the GTL process. However, due to the high cost of cobalt and noble metals, which are often employed as promoters, extending catalyst lifespan is essential to ensure the process remains economically viable. Extensive research has been conducted on oxidation as a potential deactivation mechanism of FTS catalysts [54]. One study demonstrated that oxidation is not a significant deactivation mechanism during FTS for supported Co catalysts with crystallite sizes above 2 nm. Saib et al. [54] offered recommendations for extending catalyst lifespan and preventing deactivation. To reduce catalyst costs in FTS applications, zirconium (Zr) is a promising promoter due to its ability to enhance catalyst activity via CO dissociation, promote CO reduction [55], and increase hydrocarbon selectivity [51]. Recent studies by Choodari et al. [56] explored FTS using Zr-K on iron-based catalysts. They synthesized various combinations of Zr, K, and Fe for FTS under different operating conditions. However, the use of potassium as a promoter resulted in lower C5+ selectivity and CO conversion, attributed to issues such as coking, rapid structural changes, short-chain product formation, and high olefin selectivity. In their report, the C5+ selectivity and CO conversion were 64.2% and 67.7%, respectively. For iron-based catalysts activated at high temperatures (above 380°C), many efforts have focused on reducing the activation temperature for the FTS reaction. Catalysts activated at higher temperatures face challenges, including temperature runaway and coking, during the reaction [57]. Therefore, challenges remain in catalyst preparation, particularly in synthesizing new catalysts with lower activation temperatures, higher yields, and improved stability.

Few studies have reported FTS using Co/Ce/Zr catalysts [58-60] under various catalyst preparation and operating conditions, but challenges remain in this area. The current study focused on a Co/γ-$Al_2O_3$ catalyst (referred to as Co-Al) for the FTS reaction. Zirconium and cerium were employed as promoters to enhance the catalyst's performance.

Different promoter loadings were applied to synthesize FTS catalysts. In this research, four types of catalysts were synthesized using the wet impregnation method, and characterization tests were conducted to determine the properties of the FTS catalysts. The structure of the catalysts was analyzed using X-ray Diffraction (XRD). Additionally, the Brunauer Emmet-Teller (BET) test was performed for surface area measurements, Scanning Electron Microscope (SEM) for visual observation of morphology, and Hydrogen Temperature-Programmed Reduction ($H_2$-TPR) to define the reducibility and reduction behavior of the catalysts. Finally, a reactor test was conducted to evaluate the production quality and stability of the catalysts.

## 2. Materials and Methods

### 2.1. Materials

All materials were utilized in their original form: γ-alumina (Sigma-Aldrich, 99.99%), Cobalt (II) nitrate (Co $(NO3)_2.6H_2O$, Sigma-Aldrich, 99%), Zirconium (IV) nitrate (Zr $(NO3)4.4H_2O$, Sigma-Aldrich, 99%), Cerium (III) nitrate (Ce $(NO3)3.6H_2O$, Sigma-Aldrich, 99%). The deionized water was applied for catalyst synthesis.

### 2.2. Catalyst synthesis

The wet impregnation method was used to synthesize four types of cobalt-based catalysts, following these procedures. First, γ-alumina extrusions were milled using a Retsch Planetary Ball Mill (PM 200) to produce a powder. Then, the appropriate amounts of Co $(NO3)_2·6H_2O$ and Zr $(NO3)4·4H_2O$ were dissolved in deionized water under stirring and heated to 100 °C. These solutions were then added to the γ-alumina support. In addition, the desired amount of Ce $(NO3)3·6H_2O$ was added to the mixture. Following impregnation, the samples were subjected to a drying step at 120 °C for 24 h to ensure the removal of residual moisture. Subsequently, calcination was carried out at 400 °C for 3 h in the presence of air to activate the catalysts and stabilize their structures.

### 2.3. Catalysts characterization

In this study, various analytical techniques were employed to comprehensively characterize the catalysts used in the FTS. The fresh catalyst's XRD pattern was generated using an X-ray diffractometer (Philips PW1840) equipped with monochromatized Cu (Kα) radiation. The γ-alumina and cobalt oxide phases were identified by comparing their diffraction patterns to standard patterns in the XRD library. Additionally, the crystallite size of cobalt and the support was calculated and reported using the Scherrer equation (Eq. 1):

$$D = \frac{K\lambda}{\beta \cos\theta} \quad (1)$$

In this equation, D, K, λ, β, and θ represent the following: D is crystallite size, expressed in the same unit as λ, typically in angstroms (Å) or nanometers (nm). K is shape factor, a dimensionless constant. λ is wavelength of the Kα1 radiation from the X-ray source used in the XRD measurement. B is Full Width at Half Maximum (FWHM) of the diffraction peak, which must be converted to radians before applying the equation. And θ is position of the diffraction peak on the horizontal axis of the diffraction pattern. If the horizontal axis is 2θ, the value should be divided by two to obtain θ.

Thermo-gravimetric Analysis (TGA) was employed to measure the mass change of the synthesized catalyst as a function of temperature or time under a controlled atmosphere. The analysis was conducted using a Mettler Toledo TGA/SDTA 851e instrument, with nitrogen ($N_2$) as the inert gas.

$N_2$ adsorption isotherms were utilized to determine the surface areas using the BET method (Micrometrics TriStar II, FL, USA). The pore volume, BET surface area, and average pore size of the catalyst were measured using $N_2$ physisorption on a Micrometrics ASAP 3020 automated system. The procedure involved degassing 0.5 g of the catalyst initially at 100 °C for one hour, followed by further degassing at 300 °C for two hours prior to analysis.

The morphology of the catalysts and their precursors was analyzed using a field-emission scanning electron microscope (FE-SEM Mira3 Tescan).

$H_2$-TPR was employed to evaluate the reduction temperatures of the promoted catalysts, using a Micrometrics TPD-TPR 290 system to capture their $H_2$-TPR profiles after calcination. The analysis involved using

50 mg of each sample in a gas mixture of 95% argon and 5% hydrogen, heated from 0 to 800 °C at a rate of 10 °C/min. Additionally, a Perkin Elmer Optima 8000 DV ICP (Inductively Coupled Plasma) analyzer was utilized to assess the elemental composition of the catalysts.

### 2.4. Catalyst reactor test

Fig. 1 illustrates a fixed-bed reactor used for conducting a catalytic reaction. This reactor comprises a stainless-steel tube with a 0.96 cm inner diameter and a length of 72 cm. The reactor pressure and inlet gas flow rate were adjusted using a pressure controller and a digital mass flow controller. Heat for the reaction was supplied by a heating salt bath equipped with temperature indicators and controllers. In each experimental run, 2 g of the catalyst was placed in the middle of the reactor before initiating the reaction. The catalyst bed measured 2.5 cm in long, and the reactor was operated under a continuous flow of $H_2$ at 400 °C and atmospheric pressure for 16 h. Subsequently, the catalyst was evaluated under a synthesis gas stream with an $H_2/CO$ molar ratio of 2 and a Gas Hourly Space Velocity (GHSV) of $L\cdot h^{-1}\cdot gCat^{-1}$ over a period of 70 h. The reaction temperature was gradually increased from 210 °C to 230 °C, while maintaining a constant pressure of 27 bar. The optimum operating temperature was determined to be 220 °C, as it yielded the most favorable product distribution during the FTS reaction. The reaction effluent flowed through both hot and cold traps, with the gas stream from the top directed to an online gas chromatograph (GC-Agilent 7890A) for analysis [61]. A flow diagram of the catalyst test system is provided in Fig. 1. Throughout the reaction process, product samples from the hot and cold traps were collected every 24 h [62]. The hot trap captured heavy hydrocarbon products, while the cold trap collected light hydrocarbon products. Unreacted feed gases were processed through a back-pressure regulator before analysis using a GC instrument equipped with a Flame Ionization Detector (FID) and two Thermal Conductivity Detectors (TCDs) to measure $H_2$, $CH_4$, CO, $CO_2$, and other non-condensable gases, as illustrated in Fig. 1. All experiments were conducted in triplicate, and the data are presented as the mean ± standard deviation (SD).

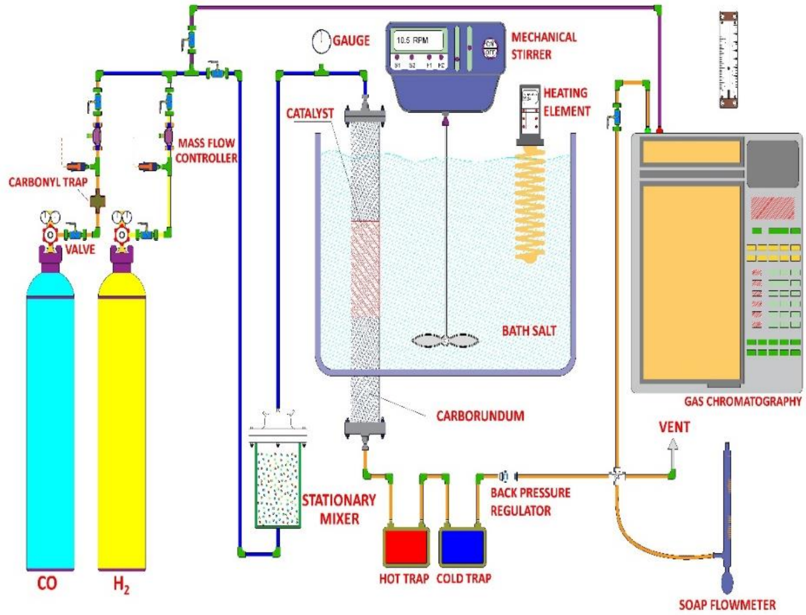


**Figure. 1.** Schematic of catalyst test system.

## 3. Result and discussion

### 3.1. XRD

Fig. 2 presents the XRD patterns of the synthesized materials with a loading of 15.0 wt%. The XRD patterns indicate the formation of dispersed Co3O4 crystals on the γ-alumina support, demonstrating a robust interaction between these two phases. Additionally, the γ-alumina support maintained its stability during the calcination process.

The introduction of Ce and Zr promoters did not markedly alter the XRD patterns, suggesting that these promoters were likely integrated into the Co3O4 structure rather than forming distinct phases.

In addition to the diffraction peaks corresponding to the cubic phase of Co3O4, the XRD patterns exhibited features suggesting the potential existence of $CoAl_2O_4$. Under certain experimental conditions, it is possible that the XRD patterns for these phases cannot be differentiated. The peaks observed at 2θ= 45.7 ° and 67 ° in the patterns can be attributed to γ-$Al_2O_3$. The current results align with previous studies [58, 59]. On the other hand, the peaks observed at 31.4 °, 36.9 °, 45.0 °, 59.5 °, and 65.5 ° were identified as belonging to the Co3O4 phase, which was present in all of the catalysts. The lack of detected Zr in the catalysts may be attributed to its high dispersion or low

concentration.
Similarly, Ce phases were not observed, potentially because Zr atoms were uniformly distributed over the support, had a relatively low concentration in the catalysts, or were incorporated into the Co3O4 lattice [58]. Overall, it appears that the addition of Zr and Ce, followed by air-drying treatment, did not significantly impact the crystalline phases of the catalysts.

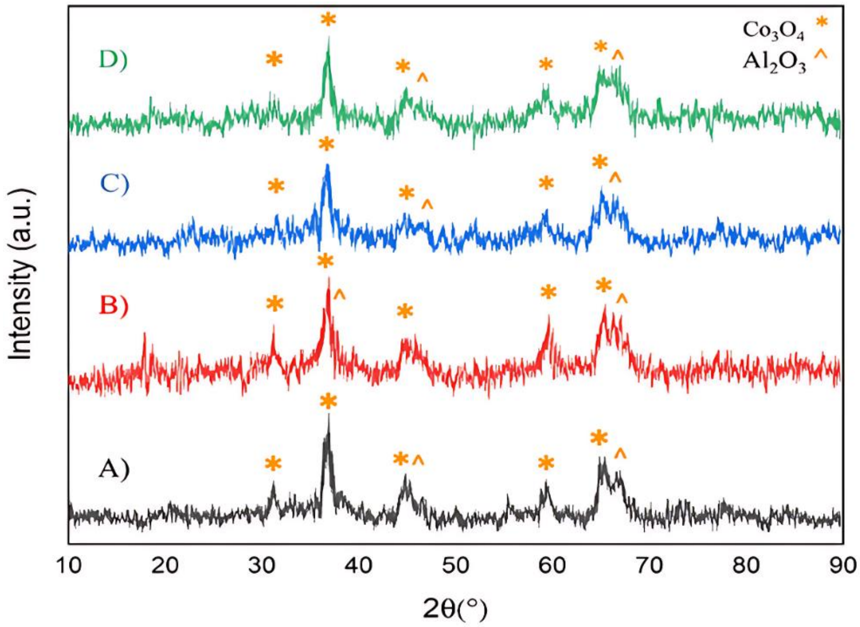


**Figure. 2.** XRD patterns of the catalysts A) 15Co/γ-$Al_2O_3$, B) 15Co/3Zr/γ-$Al_2O_3$, C) 15Co/3Ce/γ-$Al_2O_3$, D) 15Co/1.5Zr/1.5Ce/γ-$Al_2O_3$.

The crystallite sizes of Co3O4 and $Al_2O_3$ in the materials synthesized using commercial γ-$Al_2O_3$ were estimated based on the broadening of diffraction peaks in the XRD pattern. The results indicate that the incorporation of Ce into the alumina support promotes the growth of Co3O4 crystallites, increasing their size from 10.3 nm in 15Co/ γ-$Al_2O_3$ to 11.7 nm in 15Co/3Ce/γ-Al2O3, as reported in Table 1.

**Table 1.** Average crystallite size of $Co_3O_4$, and $Al_2O_3$ estimated from Scherrer equation.

| Catalysts | XRD | |
|---|---|---|
| | d ($Co_3O_4$) (nm) | d($Al_2O_3$) (nm) |
| 15Co/γ-$Al_2O_3$ | 10.3 | 15.8 |
| 15Co/3Zr/γ-$Al_2O_3$ | 11.1 | 9.8 |
| 15Co/3Ce/γ-$Al_2O_3$ | 11.7 | 8.6 |
| 15Co/1.5Zr/1.5Ce/γ-$Al_2O_3$ | 11.3 | 6.4 |

### 3.2. TGA

The TGA profile of the 15Co/γ-$Al_2O_3$, 15Co/3Zr/γ-$Al_2O_3$, 15Co/3Ce/γ-$Al_2O_3$, and 15Co/1.5Zr/1.5Ce/γ-$Al_2O_3$ catalyst under an $N_2$ atmosphere provides valuable insights into the thermal behavior, stability, and precursor decomposition of the Fischer-Tropsch catalyst, as presented in Fig. 3 and Table 2. The data indicate that the catalyst exhibits high thermal stability, making it suitable for high-temperature FTS applications. Optimizing the calcination temperature (~400 °C) is critical for ensuring complete precursor decomposition while maintaining the desired cobalt oxide phase for subsequent reduction and catalytic performance.
The initial weight loss in the temperature range of 50–200 °C corresponds to the removal of physically adsorbed moisture and volatile species. The Co/γ-Al2O3 catalyst exhibited the highest mass loss of 12 ± 2.1%, indicating a greater extent of water adsorption due to the porous nature of the alumina support. The incorporation of Zr and Ce reduced the moisture loss, as observed in the Co-Zr/γ-$Al_2O_3$ and Co-Zr-Ce/γ-$Al_2O_3$ catalysts, which exhibited a lower weight loss of 8%. The Co-Ce/γ-$Al_2O_3$ system, however, showed a slightly higher loss of 9%, suggesting that Ce enhances surface hydroxylation, leading to increased water retention. Between 200 and 400 °C, the most significant weight loss occurred, corresponding to the thermal decomposition of precursor nitrates and the formation of metal oxides. The Co/γ-$Al_2O_3$ catalyst exhibited the highest weight loss of 23%, reflecting the complete decomposition of cobalt nitrate and the formation of Co3O4. The presence of Zr and Ce reduced the decomposition extent, as observed in the Co-Zr/γ-$Al_2O_3$ and Co-Ce/γ-$Al_2O_3$ catalysts, which exhibited weight losses of 17%. The lowest weight loss in this range was observed for the Co-Zr-Ce/γ-$Al_2O_3$ catalyst (16%), indicating that the combined effect of Zr and Ce enhances precursor stability and delays the onset of thermal decomposition.

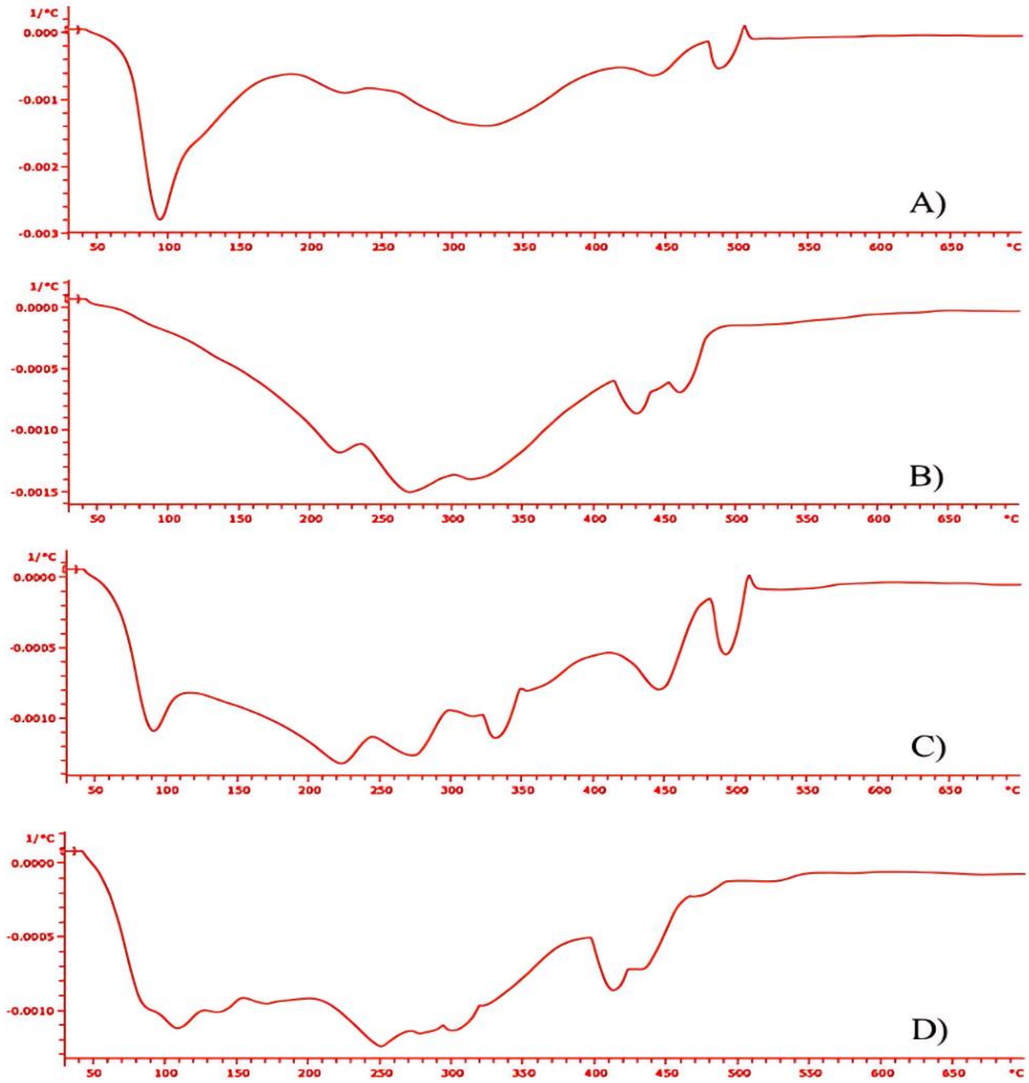


**Figure. 3.** TGA pattern of catalysts: A) 15Co/γ-$Al_2O_3$, B) 15Co/3Zr/γ-$Al_2O_3$, C) 15Co/3Ce/γ-$Al_2O_3$, D) 15Co/1.5Zr/1.5Ce/γ-$Al_2O_3$.

The temperature range of 400–500 °C corresponds to the phase transition of metal oxides, particularly the reduction of $Co_3O_4$ to CoO and the stabilization of $ZrO_2$ and $CeO_2$. In this range, all catalysts exhibited similar weight loss behavior, with values ranging between 5–6%. The slightly higher weight loss observed in the Co-Ce/γ-$Al_2O_3$ and Co-Zr-Ce/γ-$Al_2O_3$ catalysts (6%) suggests that Ce plays a role in structural reorganization during oxide formation. At temperatures exceeding 500 °C, there was minimal weight loss, which indicates that the catalysts stabilized in their final oxide forms. The Co/γ-$Al_2O_3$ catalyst had the lowest residual mass (56.24%), confirming that γ-$Al_2O_3$ alone does not provide significant thermal stability at high temperatures. The incorporation of Zr significantly improved stability, as evidenced by the Co-Zr/γ-$Al_2O_3$ catalyst, which exhibited the highest final residual mass of 63.09%. The Co-Ce/γ-$Al_2O_3$ catalyst exhibited a slightly lower final residual mass of 60.82%, indicating that Ce improves thermal resistance but is less effective than Zr in stabilizing the catalyst structure. The Co-Zr-Ce/γ-$Al_2O_3$ catalyst showed a final residual mass of 61.99%, demonstrating a synergistic effect between Zr and Ce in improving the high-temperature stability of the catalyst. Overall, the comparative analysis reveals that the monometallic Co/γ-$Al_2O_3$ catalyst undergoes the most significant decomposition and has the lowest thermal stability, making it less suitable for high-temperature catalytic applications. Zr enhances precursor stability and high-temperature resistance, with Co-Zr/γ-$Al_2O_3$ demonstrating the highest residual mass. The incorporation of Ce influences both moisture adsorption and phase transformation behavior, as observed in the Co-Ce/γ-$Al_2O_3$ catalyst. The Co-Zr-Ce/γ-$Al_2O_3$ system exhibits an optimal balance between precursor decomposition stability and high-temperature structural retention, making it a promising candidate for FTS process. The results show that the selection of promoters significantly influences the thermal behavior of the catalyst, with Zr and Ce collectively improving both precursor stability and thermal resistance at high temperatures.

**Table 2.** TGA results for the catalysts: A) 15Co/γ- $Al_2O_3$, B) 15Co/3Zr/γ- $Al_2O_3$, C) 15Co/3Ce/γ- $Al_2O_3$, and D) 15Co/1.5Zr/1.5Ce/γ- $Al_2O_3$.

| Catalyst | Moisture loss % (50-200°C) | Precursor decomposition% (200-400°C) | Phase transition % (400-500°C) | Stabilization and residual loss % (500-650°C) | Final residual mass % |
|---|---|---|---|---|---|
| 15Co/γ-$Al_2O_3$ | 12.0 | 23.0 | 5.0 | 3.76 | 56.24 |
| 15Co/3Zr/γ-$Al_2O_3$ | 8.0 | 17.0 | 5.0 | 6.91 | 63.09 |
| 15Co/3Ce/γ-$Al_2O_3$ | 9.0 | 17.0 | 6.0 | 7.18 | 60.82 |
| 15Co/1.5Zr/1.5Ce/γ-$Al_2O_3$ | 8.0 | 16.0 | 6.0 | 8.0 | 61.99 |

### 3.3. $H_2$-TPR

The reducibility and reduction behavior of the catalysts were analyzed through $H_2$-TPR tests, with the results displayed in Fig. 4. Indeed, cerium serves as a catalyst in the reduction process, enabling the movement of electrons and facilitating their transfer from the reducing agent to the $Co_3O_4$ surface. This procedure is essential in catalytic applications because it improves the selectivity and efficiency of the catalyst. The reduction behavior of catalyst samples, which included varying amounts of Zr and Ce, was evaluated using $H_2$-TPR analysis. Fig. 3 reveals distinct reduction peaks for Co/γ-$Al_2O_3$ at different temperature ranges: <200°C, 200–650°C, and >650°C. The first peak corresponds to the reduction of $Co_3O_4$ to CoO, while the broader peak at higher temperatures indicates the further reduction of CoO to metallic cobalt (Co). These distinct peaks at different temperatures suggest associations between the metal and the support in each catalyst. Additionally, a minor peak below 300°C is observed, likely arising from the reductive decomposition of residual Co $(NO_3)_2$ on the catalysts. Moreover, some catalysts show broad peaks in the second reduction step, indicating different degrees of interaction between cobalt and the support. It is also possible that cobalt aluminate may be present, which typically reduces at temperatures above 1000°C. Among the examined catalysts, catalyst D exhibited the most pronounced reduction behavior, as evidenced by its distinct reduction peaks and interaction characteristics. By comparing the current results with previous studies [56, 57, 63] on the iron-based catalyst, it was demonstrated that the cobalt-based catalyst is activated at a lower temperature, thus preventing temperature runaway and coking issues during the reaction.

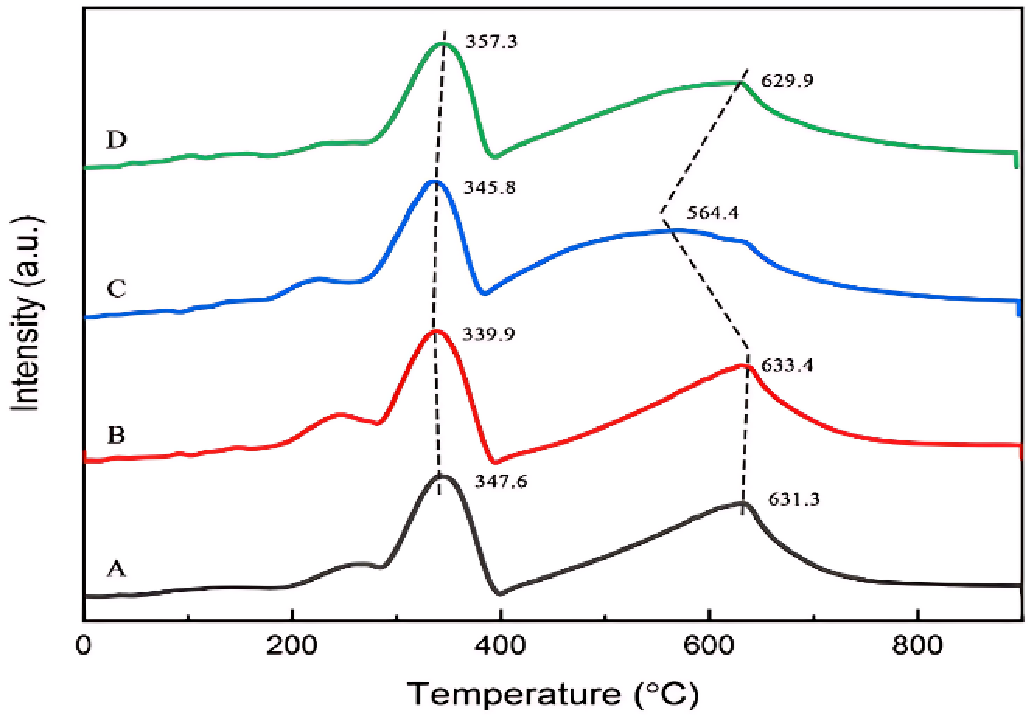


**Figure. 4.** $H_2$-TPR patterns of the catalysts A) 15Co/γ- $Al_2O_3$, B) 15Co/3Zr/γ- $Al_2O_3$, C) 15Co/3Ce/γ- $Al_2O_3$, D) 15Co/1.5Zr/1.5Ce/γ- $Al_2O_3$.

Fig. 5 illustrates the reduction of the cobalt catalyst in two distinct stages of the reduction process. The first peak corresponds to the reduction of $Co_3O_4$ to CoO, while the second peak is associated with the subsequent reduction of CoO to metallic cobalt (Co). A small peak observed at 200–300°C, preceding the two main peaks, is attributed to residual metal nitrate salts that were not fully converted into metal oxides during the calcination stage. Consequently, the reduction of $Co_3O_4$ to CoO shifts to higher temperatures when the catalyst contains Zr and Ce.

The area under the curve represents the volume of hydrogen uptake, which directly correlates with the reduction process. A lower reduction temperature and increased hydrogen uptake indicate enhanced reducibility. As evidenced by the TPR profiles, the presence of promoters leads to a more pronounced decrease in reduction temperatures. These findings confirm that promoted catalysts achieve a higher degree of reduction. Since the reduction of $Co_3O_4$ to Co is a critical step in this process, the introduction of promoters can influence the temperature at which this transformation occurs. A shift to higher temperatures may indicate reduced catalyst reducibility, which could potentially affect its overall activity.

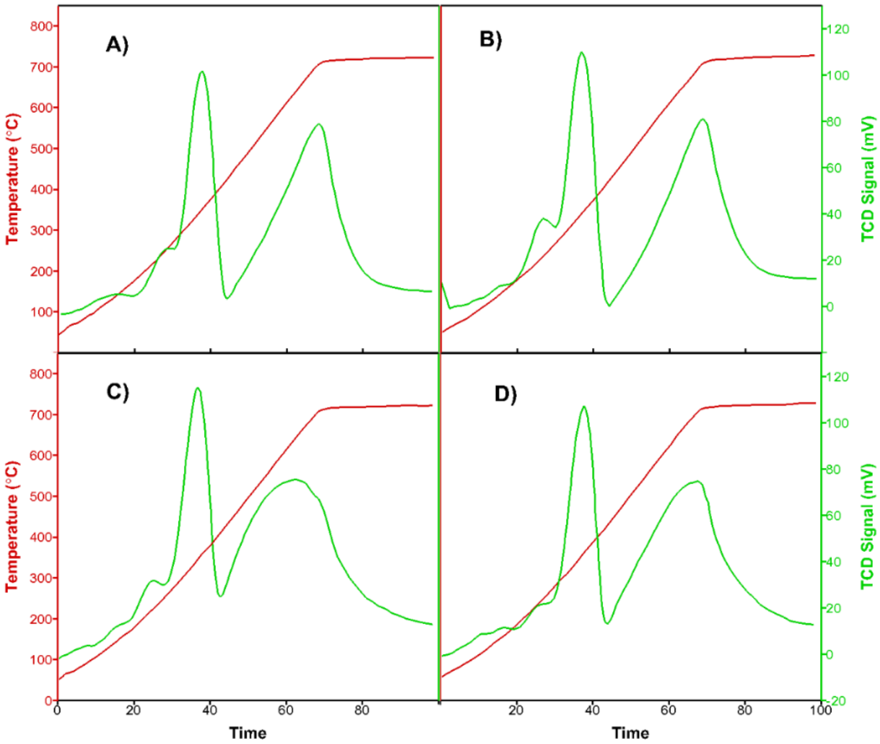


**Figure. 5.** $H_2$-TPR profile of catalysts: A) 15Co/γ-$Al_2O_3$, B) 15Co/3Zr/γ-$Al_2O_3$, C) 15Co/3Ce/γ-$Al_2O_3$, D) 15Co/1.5Zr/1.5Ce/γ-$Al_2O_3$.

Table 3 presents the quantitative data on hydrogen consumption by the catalysts. The lowest hydrogen consumption was noted for the Co/γ-$Al_2O_3$ catalyst. These findings indicate that the presence of the promoter helps to increase hydrogen uptake. The Co/Ce/Zr/γ-$Al_2O_3$ catalyst showed the highest hydrogen consumption. This suggests that the addition of Zr and Ce to the catalyst improved the distribution of the $Co_3O_4$ phase, thereby enhancing the hydrogen spillover effect. This effect occurs when hydrogen molecules dissociate on a catalyst's surface and move to adjacent sites, reacting with other molecules, which increases the number of active sites for catalytic reactions. Consequently, the catalysts containing 1.5%Zr and 1.5%Ce are presumed to exhibit superior catalytic activity due to better dispersion of the $Co_3O_4$ phase, facilitating more effective hydrogen spillover. This process leads to enhanced nucleation and more efficient surface oxide reduction.

**Table 3.** $H_2$-TPR results of the catalysts A) 15Co/γ-$Al_2O_3$, B) 15Co/3Zr/γ-$Al_2O_3$, C) 15Co/3Ce/γ-$Al_2O_3$, D) 15Co/1.5Zr/1.5Ce/γ-$Al_2O_3$.

| Catalysts | Temperature peak (°C) | $H_2$/g (mmol) | Total $H_2$ consumption (mmol) |
|---|---|---|---|
| A | 347.6 | 1.23 | 0.04 |
| | 704.4 | 1.84 | 0.06 |
| B | 339.9 | 1.37 | 0.05 |
| | 706.1 | 1.65 | 0.06 |
| C | 357.3 | 1.19 | 0.04 |
| | 704.5 | 2.38 | 0.08 |
| D | 345.8 | 1.56 | 0.05 |
| | 640.5 | 2.82 | 0.09 |

### 3.4. $N_2$ Physiosorption

Table 4 presents the surface area, average pore diameter, and pore volume of the promoters and cobalt catalysts. The results clearly indicate that the BET surface area of the support is 217.1 $m^2/g$, which decreases to 147.1 $m^2/g$ for the 5Co/γ-$Al_2O_3$ catalyst. However, a slight increase was observed when the catalyst was promoted with 3 wt% Zr and Ce, while the pore size slightly decreased. This reduction in pore size can be attributed to the presence of $Co_3O_4$ clusters, which may cause pore blockage. The decrease in specific surface area, pore size, and pore volume of the catalysts after metal loading indicates that Co and Ce are well mixed with the porous structure of the catalysts. Pardo et al. [59] reported a similar pattern of partial coverage of the mesopores by Ce species on the γ-$Al_2O_3$ support. However, the catalysts' pore volume and specific surface area decreased compared to $Co_3O_4$, which aligns with previous studies. Including Zr and Ce promoters noticeably impacts the surface area and pore volume. The impregnation of cobalt and promoters slightly reduces the pore size in the 15Co/3Zr/γ-$Al_2O_3$ and 15Co/3Ce/γ-$Al_2O_3$ catalysts, while the pore volume remains unchanged. This suggests that some cobalt species and promoters entered the pores of the supports and blocked them, resulting in a decrease in available surface area and pore volume [7, 58, 60]. Furthermore, the incorporation of 3 wt% Zr, 3 wt% Ce, or a combination of 1.5 wt% Zr and 1 wt% Ce led to a decrease in surface area, which is likely attributable to a synergistic interaction between the dopants.

**Table 4.** BET, pore volume, and pore size of the support and the cobalt-based catalysts before reaction: A) 15Co/γ- $Al_2O_3$, B) 15Co/3Zr/γ-$Al_2O_3$, C) 15Co/3Ce/γ- $Al_2O_3$, D) 15Co/1.5Zr/1.5Ce/γ- $Al_2O_3$.

| Catalysts & Support | BET ($m^2/g$) | Pore volume ($cm^3/g$) | Pore size (nm) |
|---|---|---|---|
| γ-$Al_2O_3$ | 217.1 | 0.512 | 9.54 |
| A | 147.1 | 0.443 | 12.00 |
| B | 155.4 | 0.454 | 11.60 |
| C | 155.4 | 0.448 | 11.51 |
| D | 149.4 | 0.449 | 12.01 |

The significant decrease in BET surface area after the FTS reaction can be attributed to a combination of factors that affect the catalyst structure during operation that was presented in Table 5. High reaction temperatures and prolonged reaction times can lead to sintering of the active cobalt particles as well as the support, which results in the growth of particles and a consequent reduction in the available surface area. In addition, the reaction conditions may promote the formation of coke on the catalyst surface, effectively blocking the pores and further reducing the measurable surface area. This effect is observable across all four catalysts, although the extent of reduction exhibits slight variations depending on the specific promoter employed. For example, the catalyst promoted with cerium (15Co/3Ce/γ-$Al_2O_3$) shows a more pronounced decrease, suggesting that the presence of cerium might have influenced the extent of sintering or coking differently compared to zirconium or the unpromoted catalyst. Overall, these changes are typical for catalysts under harsh reaction conditions, where both physical sintering and chemical fouling contribute to the loss of surface area observed in the BET analysis after the test.

**Table 5.** BET, pore volume, and pore size of the support and the cobalt-based catalysts after reaction: A) 15Co/γ-$Al_2O_3$, B) 15Co/3Zr/γ-$Al_2O_3$, C) 15Co/3Ce/γ-$Al_2O_3$, D) 15Co/1.5Zr/1.5Ce/γ-$Al_2O_3$.

| Catalysts & Support | BET ($m^2/g$) | Pore volume ($cm^3/g$) | Pore size (nm) |
|---|---|---|---|
| A | 76.16 | 0.281 | 14.8 |
| B | 97.13 | 0.340 | 14.0 |
| C | 53.88 | - | - |
| D | 67.61 | 0.242 | 14.3 |

In addition, Fig. 6 displays the adsorption and desorption isotherms of the catalysts at 77K, which are identified as type IV according to the Brunauer–Deming–Deming–Teller (BDDT) classification, indicative of mesoporosity in all samples at high relative pressures (p/p0). Capillary condensation occurs in the p/p0 range of 0.6–0.8, confirming their mesoporous characteristics.

### 3.5. Inductively Coupled Plasma (ICP)

ICP analysis was conducted to verify the composition of elements in the catalysts. Table 6 shows that the compositions determined by ICP closely match those of the synthesis solutions. The results of this analysis align with theoretical expectations, indicating that the precursor salts $Co(NO_3)_2·6H_2O$, $Ce(NO_3)_3·6H_2O$, and $Zr(NO_3)_4·4H_2O$, are completely reduced during the liquid phase of the co-reduction process.

**Table 6.** ICP analysis of the catalyst: A) 15Co/γ-$Al_2O_3$, B) 15Co/3Zr/γ-$Al_2O_3$, C) 15Co/3Ce/γ-$Al_2O_3$, D) 15Co/1.5Zr/1.5Ce/γ-$Al_2O_3$.

| Catalyst | Al (wt%) | Co (wt%) | Ce (wt% | Zr (wt%) |
|---|---|---|---|---|
| A | 32.454 | 18.565 | _ | _ |
| B | 32.651 | 18.235 | _ | 4.325 |
| C | 32.325 | 18.627 | 4.832 | _ |
| D | 33.265 | 19.165 | 4.198 | 2.524 |

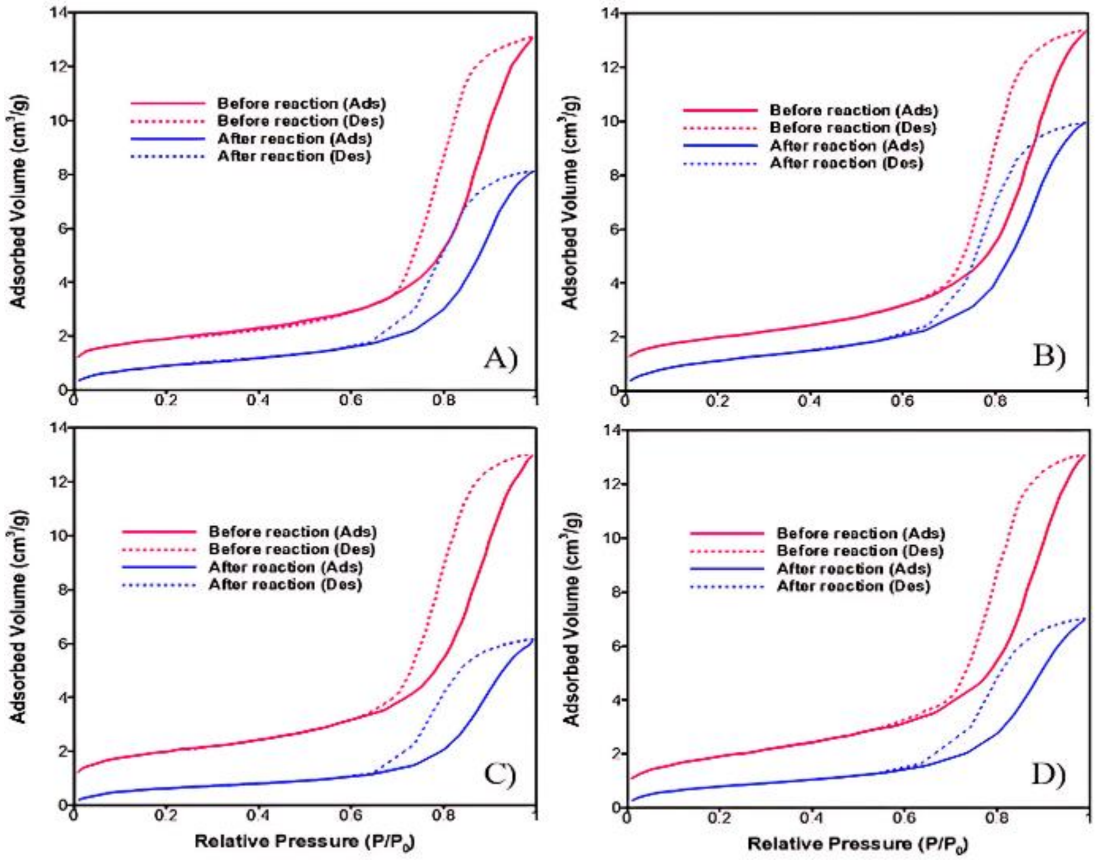


**Figure. 6**. $N_2$ adsorption-desorption isotherms for the catalysts: A) 15Co/γ-$Al_2O_3$, B) 15Co/3Zr/γ-$Al_2O_3$, C) 15Co/3Ce/γ-$Al_2O_3$, D) 15Co/1.5Zr/1.5Ce/γ-$Al_2O_3$ before and after reaction.

## SEM

Fig. 7 presents typical SEM images of the catalysts. The size and morphology of the catalyst particles significantly influence their catalytic performance, affecting key factors such as surface area, pore accessibility, and active sites. The images reveal that the catalyst particles exhibit a distinctive structure, consisting of randomly crumpled and wrinkled sheets [64, 65]. The SEM images also show the catalyst pore diameter size range is between 5–18 nm. The corresponding mean pore diameter for the catalysts A, B, C and D are 13, 8.42, 12.21 and 7.96 nm, respectively. The decrease in mean pore size upon the addition of Zr and Ce promoters to the 15Co/γ-$Al_2O_3$ catalyst can be explained by several structural and physicochemical effects. One of the primary reasons for this reduction is the partial blocking of pores due to the deposition of Zr and Ce within the porous structure of γ-$Al_2O_3$. These promoters, when incorporated into the catalyst, tend to distribute over the surface or inside the pores, effectively reducing the overall pore volume and diameter. This phenomenon is particularly evident in the catalysts containing Zr, where the mean pore size decreases significantly from 13 nm in the unpromoted catalyst to 8.42 nm in the 15Co/3Zr/ γ-$Al_2O_3$ sample and further to 7.63 nm in the 15Co/1.5Zr/1.5Ce/γ-$Al_2O_3$ sample. The presence of Zr, therefore, plays a more pronounced role in narrowing the pores.

Additionally, the formation of metal oxides, such as $ZrO_2$ and $CeO_2$, contributes to this effect. These oxides tend to disperse finely over the γ-$Al_2O_3$ surface, filling the pore structure and effectively decreasing the average pore diameter. Since $ZrO_2$ has a smaller particle size and higher dispersion capability than $CeO_2$, it has a stronger impact on pore size reduction. This is reflected in the fact that the 15Co/3Ce/γ-$Al_2O_3$ catalyst, exhibits a mean pore size of 12.21 nm, which is closer to the unpromoted catalyst. The difference in pore size reduction between the Zr- and Ce-containing samples suggests that Zr is more effective at modifying the porosity of the support material. Moreover, the incorporation of Zr and Ce enhances the metal-support interaction, which leads to better dispersion of cobalt particles. This strong interaction, particularly in Zr-containing catalysts, facilitates the formation of Co-O-Zr and Co-O-Ce bonds, which in turn contribute to the narrowing of the pores by stabilizing smaller metal particles within the support. The presence of these promoters may also cause slight structural rearrangements within the alumina framework, leading to a contraction of pore dimensions. This effect is more pronounced in the 15Co/1.5Zr/1.5Ce/γ-$Al_2O_3$ catalyst, where the combination of both promoters results in the most significant reduction in pore size. Our findings are in line with previous studies [59, 66].

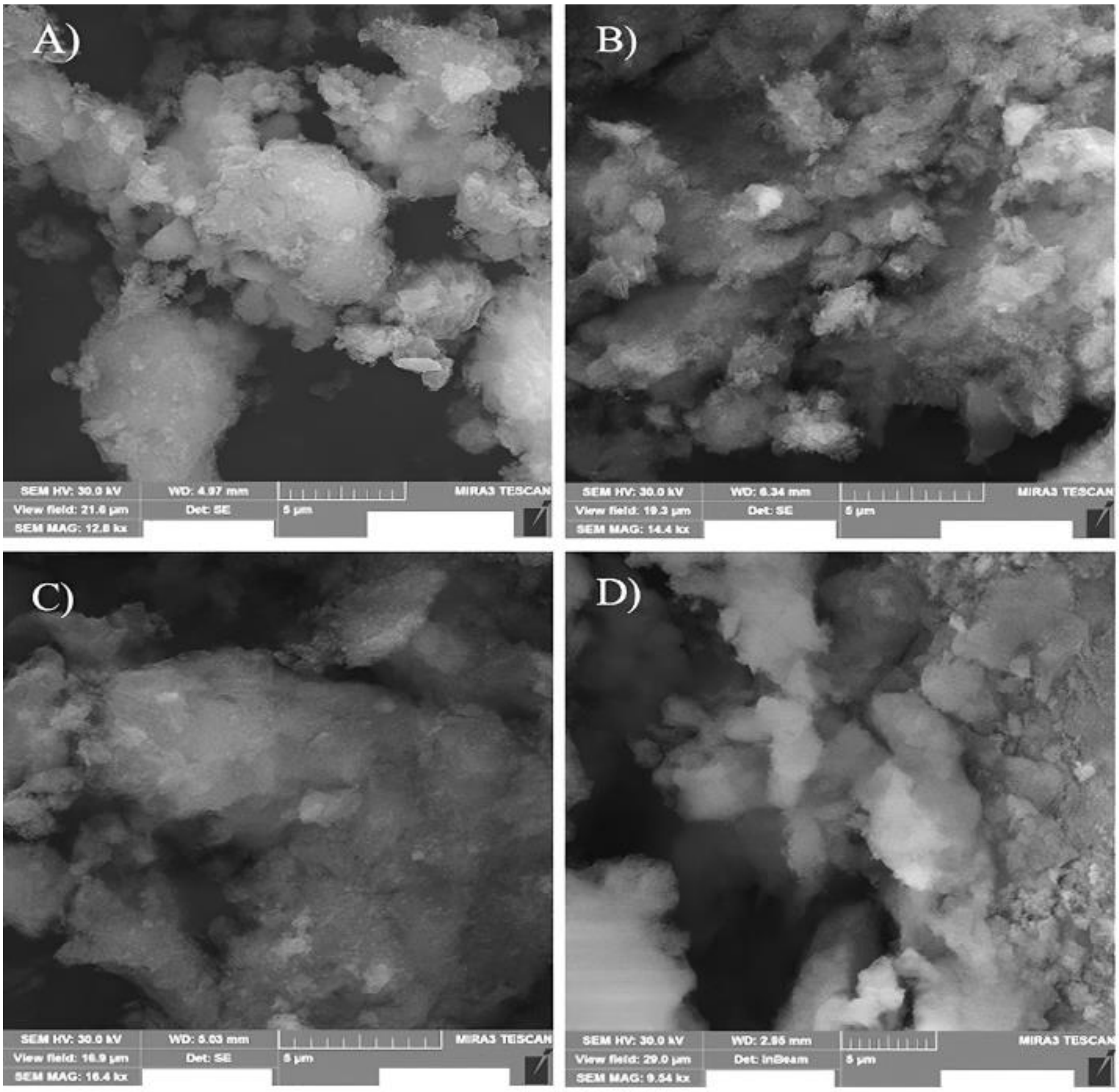


**Figure. 7.** SEM images of the catalysts A) 15Co/γ-$Al_2O_3$, B) 15Co/3Zr/γ- $Al_2O_3$, C) 15Co/3Ce/γ- $Al_2O_3$, D) 15Co/1.5r/1.5Ce/γ- $Al_2O_3$.

### 3.7. FTS performance

A comparison between previous studies and the current work, as presented in Table 7, confirms that the synthesized catalysts' performance, including Fischer–Tropsch Yield (FTY) and selectivity, demonstrates remarkable improvements. The results indicate that the catalyst co-promoted with Zr and Ce exhibited enhanced reduction behavior and superior reactor performance, as evidenced by a higher C5+ selectivity compared to the unpromoted catalyst. As a result of the metal-support interaction, the addition of promoters enhances the dispersion of active metals in FTS. Consequently, incorporating Zr and Ce into the cobalt-based catalyst led to a greater yield of hydrocarbons with higher molecular weights. These findings indicate that incorporating promoters into the catalysts enhances the chain growth reaction while limiting the hydrogenation reaction.

The single-promoted catalyst exhibited the opposite effect. The $C_5^+$ selectivity of the Zr/Ce-promoted catalyst was 82.3 ± 0.9%, which was higher than that of the unpromoted catalyst. In addition, the 15Co/3Zr and 15Co/3Ce catalysts, which exhibit synergistic effects of the two promoters, achieved $C_5^+$ yields of 77.5 ± 1.8% and 73.5 ± 1.8%, respectively. Based on empirical results, promoters like Zr accelerated C5+ selectivity and enhanced catalyst activity. These impacts can be attributed to two significant contributions: First, the presence of Zr-rich phases reduces the synthesis of Co/Al spinel compounds while increasing the availability of active Co sites. Second, acidic sites linked with Zr promote selectivity for longer-chain hydrocarbons [58]. This explains why catalyst B exhibits higher $C_5^+$ selectivity compared to catalyst C. Our findings align with previous research [4, 56, 67, 68]. Additionally, Ce increases the oxygen storage capacity of the catalyst. The results indicate that catalysts with higher Ce loading presented lower selectivity toward long-chain hydrocarbon formation and increased selectivity toward CH4 and $CO_2$. Comparing $CO_2$ selectivity between catalysts B and C reveals that the $CO_2$ selectivity of catalyst C (1.65%) is higher than that of catalyst B (1.16 %). On the other hand, the presence of $CeO_2$ on the support surface enhances the reducibility of cobalt oxides, lowering the reduction temperature by approximately 70 °C [60, 69, 70]. The olefin/paraffin (O/P) ratio for all catalysts ranged from 1.1 to 2.4.

**Table 7.** Comparison of product selectivity of the present study with previous works: A) 15Co/γ-$Al_2O_3$, B) 15Co-3Zr/γ-$Al_2O_3$, C) 15Co-3Ce/γ-$Al_2O_3$, D) 15Co-1.5Zr-1.5Ce/γ-$Al_2O_3$).

| Catalysts | P (bar) | T (°C) | $H_2$/CO | GHSV ($L.h^{-1}$. g $Cat^{-1}$) | $C_1$ | $C_2$-$C_4$ | $C_5^+$ | $CO_2$ | CO Conversion (%) | Ref. |
|---|---|---|---|---|---|---|---|---|---|---|
| Co/$Al_2O_3$ | 19 | 225 | 2 | 0.64 | 16.1 | 16.4 | 67.6 | - | 58.4 | [7] |
| Co/$Al_2O_3$/Ba | 19 | 225 | 2 | 0.64 | 14.8 | 12.3 | 72.9 | - | 57.1 | [7] |
| Co/MCM | 9 | 199 | 2 | 1 | 33 | 35.6 | 31.4 | - | 4.8 | [8] |
| Co/SBA | 9 | 199 | 2 | 1 | 21.1 | 23.9 | 55 | - | 17.7 | [8] |
| Co/$SiO_2$ | 20 | 220 | 2 | 1.8 | 12.5 | 12.8 | 73.3 | 1.3 | 13.3 | [72] |
| Co/$SiO_2$/Pt | 20 | 220 | 2 | 1.8 | 9 | 10 | 80.4 | 0.6 | 30.5 | [72] |
| Co/$SiO_2$/Ag | 20 | 220 | 2 | 1.8 | 7.9 | 13.8 | 78.1 | 0.5 | 37.6 | [72] |
| Co/$TiO_2$ | 20 | 220 | 2 | 6 | 6.5 | 11.3 | 81.9 | 0.3 | 29.8 | [7] |
| Co/$TiO_2$/Pt | 20 | 220 | 2 | 6 | 4.9 | 6.8 | 86.3 | 2 | 45.3 | [7] |
| Co/HZSM | - | 234 | - | 3.7 | - | 32.9 | - | 1.5 | 21.3 | [7] |
| Co/HZSM/Ru | - | 234 | - | 3.7 | - | 32 | - | 3.9 | 25.4 | [15] |
| Co/HZSM/Ni | - | 234 | - | 3.7 | - | 35.8 | - | 0.2 | 35.8 | [15] |
| Co/$Al_2O_3$ | - | - | - | - | 7.9 | 9.6 | 81.8 | 0.7 | 47.7 | [16] |
| Co/$Al_2O_3$/Ag | - | - | - | - | 7.6 | 9.6 | 82.1 | 0.7 | 46.7 | [16] |
| Co/γ-$Al_2O_3$/Zr/Ce | - | 210 | 2 | 8.4 | 9.4 | - | 81 | - | - | [18] |
| A | 27 | 220 | 2 | 4 | 24.35 | 8.85 | 64.4 | 2.43 | 33.1±0.6 | P.W* |
| B | 27 | 220 | 2 | 4 | 16.79 | 4.52 | 77.5 | 1.16 | 35.9±3.2 | P.W |
| C | 27 | 220 | 2 | 4 | 15.81 | 9.24 | 73.3 | 1.65 | 44.8±1.1 | P.W |
| D | 27 | 220 | 2 | 4 | 11.59 | 4.76 | 82.3 | 1.34 | 50.4±1.5 | P.W |

Fig. 8 shows the results of yield and CO conversion, which were analyzed using GC. The incorporation of a promoter enhances both CO conversion and yield. To compute the catalyst yield, CO conversion is multiplied by selectivity. The Co/γ-$Al_2O_3$ catalyst exhibited the lowest CO conversion, likely due to the strong interaction between Co and γ-$Al_2O_3$, which limits reducibility. Consequently, the yield is affected by CO conversion and $C_5^+$ selectivity. The yield is calculated using the following Eq. (2):

$$\text{Yield} = \text{CO Conversion (\%)} \times \text{C5+ Selectivity} \qquad (2)$$

The Co/Zr/Ce catalyst achieved a higher CO conversion compared to the singly-promoted variants such as Co/Zr, and Co/Ce. Specifically, the Co/Zr/Ce catalyst reached a yield of 41.5 ± 0.8% and CO conversion of 50.4 ± 1.5%, whereas the Co/Ce catalyst recorded a yield of 32.8 ± 2.6% and CO conversion of 44.8 ± 1.1%. In comparison, the Co/Zr catalyst achieved a yield of 27.9 ± 1.2% and CO conversion of 35.9 ± 3.2%.

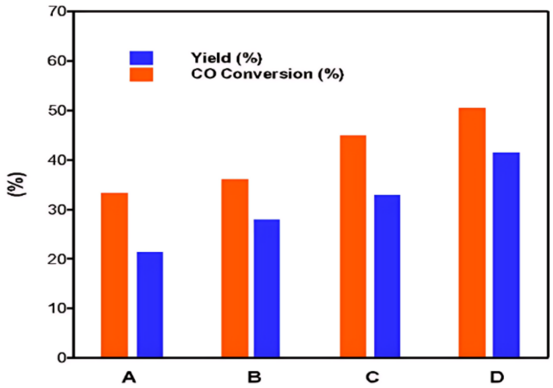


**Figure. 8.** CO conversion and yield of the catalysts A) 15Co/γ- $Al_2O_3$, B) 15Co/3Zr/γ- $Al_2O_3$, C) 15Co/3Ce/γ- $Al_2O_3$, D) 15Co/1.5Zr/1.5Ce/γ-$Al_2O_3$.

Fig. 9 illustrated the trend of CO conversion over time for the cobalt-based catalysts at 220ºC and 27 bar in terms of time on stream (TOS) for 70 h. The results show that the conversion rate of CO decreases over time and after 70 h.

Among catalysts, 15Co/1.5Zr/1.5Ce/γ-$Al_2O_3$ exhibits the highest stability.

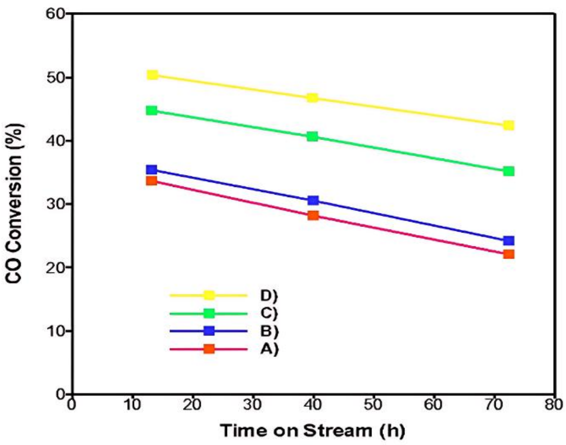


**Figure. 9.** CO conversion with time on-stream on the catalysts (220°C, 27 bar, GHSV = 2 L.h-1. gCat -1, $H_2$/CO=2.0) A) 15Co/γ- $Al_2O_3$, B) 15Co/3Zr/γ- $Al_2O_3$, C) 15Co/3Ce/γ- $Al_2O_3$, D) 15Co/1.5Zr/1.5Ce/γ-$Al_2O_3$.

Based on the $H_2$-TPR results, reactor test data, and the synergistic effect of the promoters (Zr and Ce), the stability estimation confirms that catalyst D demonstrates acceptable performance during the reactor test.

A histogram of the product distribution (categorized by carbon number) for each catalyst is illustrated in Fig. 10. This histogram emphasizes the influence of the promoter loading on the product distribution. The results of introducing a promoter clearly indicate a significant shift in the product distribution towards heavier hydrocarbons, as illustrated in Fig. 10. The distribution of hydrocarbons produced in the FTS is defined by following Eq. (3):

$$\log W_n/n = n \log \alpha + const. \qquad (3)$$

which Wn represents the mass fraction of a hydrocarbon, n is the number of carbon atoms, α is a parameter often referred to as the chain growth probability and "const" is a constant that adjusts the base level of the logarithmic function.

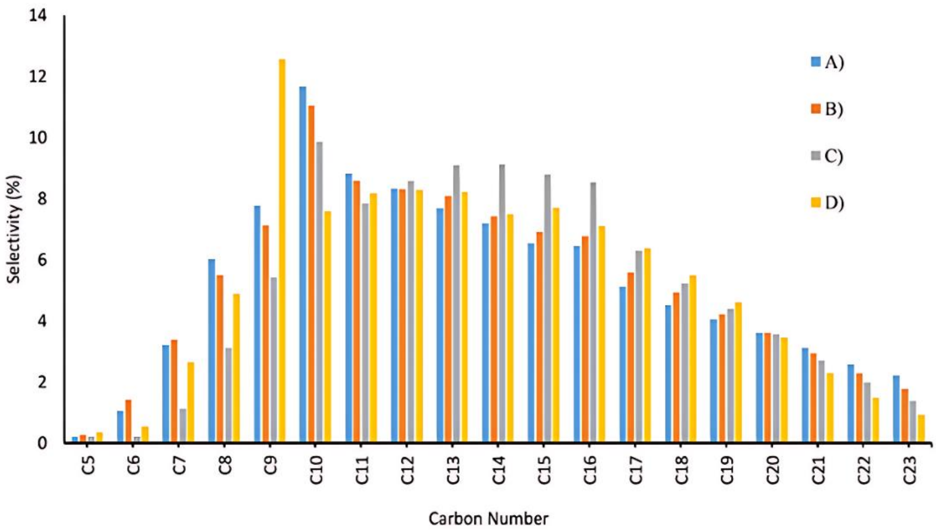


**Figure. 10.** Liquid product distribution of the catalysts A) 15Co/γ-$Al_2O_3$, B) 15Co/3Zr/γ- $Al_2O_3$, C) 15Co/3Ce/γ- $Al_2O_3$, D) 15Co/1.5Zr/1.5Ce/γ- $Al_2O_3$.

In conclusion, adding Zr and Ce promoters to the Co/γ-$Al_2O_3$ catalysts significantly improved their CO conversion and selectivity towards higher hydrocarbon products. These promoters enhanced cobalt dispersion and reducibility and favored CO dissociation, leading to higher chain growth probability and improved catalytic performance in the FTS. The findings of this study contribute to a better understanding of the role of promoters in cobalt-based catalysts for FTS and offer potential avenues for further optimizing catalyst design for efficient hydrocarbon production.

Table 7 provides valuable insights into the catalysts' α factor and selectivity trends. Catalyst D demonstrated a higher α factor than the other catalysts, indicating a higher probability of chain growth and the production of longer-chain hydrocarbons. However, the addition of $CeO_2$ led to a decrease in $C_5^+$ selectivity and the α factor. This phenomenon could be attributed to the reduction in active sites caused by $CeO_2$ loading, which may hinder the chain growth process and favor the production of lower molecular weight hydrocarbons.

The reactor test data for all four catalysts revealed an interesting finding: a linear relationship between $CH_4$ selectivity and $C_5^+$ selectivity, as depicted in Fig. 11. The correlation between $CH_4$ and $C_5^+$ selectivity was observed under fixed process conditions. This linear relationship suggests the presence of a common monomer that contributes to the formation of both $CH_4$ and higher hydrocarbons. This finding is significant, as it illustrates the interdependence between $CH_4$ and $C_5^+$ selectivity, regardless of the specific properties of Co-based catalysts, such as cobalt crystallite size, support pore size, and type of support. The identified linear relationship between $CH_4$ and $C_5^+$ selectivity provides valuable insights into the mechanistic aspects of the FTS process and the role of catalysts in hydrocarbon production. These results align with prior findings, reinforcing the reliability of the observations [71].

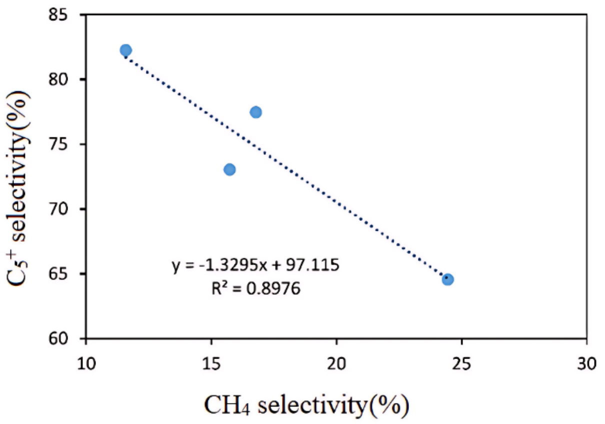


**Figure. 11.** Correlation between $CH_4$ and $C_5^+$ selectivity for the catalysts.

## 4. Conclusions

This study investigated the effect of Ce and Zr promoters on the performance of cobalt-based catalysts in an FTS reactor. The characteristic test of all prepared catalysts hit the new value of 149m$^2$/g, which was higher than that of previous studies. The combination of Ce and Zr promoters enhances hydrocarbon chain growth, thereby increasing selectivity towards longer-chain alkanes and olefins. The capacity of Ce to oscillate between multiple oxidation states facilitates the removal of coke, thereby markedly improving the catalyst's durability and potential for regeneration. In this combination, Zr increases thermal stability and resistance to sintering during the reaction, which is crucial for long-term operation at high temperatures. According to the fixed-bed reactor results, the 15Co/1.5Ce/1.5Zr/γ-$Al_2O_3$ catalyst exhibited maximum activity due to the synergistic interaction of Ce and Zr, with a productivity of 0.223 g hydrocarbon·h$^{-1}$·gCat$^{-1}$. This is particularly useful in applications where heavier synthetic fuels are desired. The GC results confirm that lower methane selectivity, advantageous for maximizing liquid fuel production, was achieved using the doubly-promoted catalyst, with CO conversion, $C_5^+$ selectivity, and yield of approximately 50.4 ± 1.5%, 82.3 ± 0.9%, and 41.5 ± 0.8%, respectively. The TPR analysis demonstrates that Zr helps distribute Co uniformly over the support, increasing the metal's exposed surface area available for the reaction. Additionally, the $H_2$-TPR analysis shows that doubly-promoted catalysts exhibited a favorable degree of reduction and dispersion, highlighting the synergistic effect between Zr and Ce promoters. Finally, the 15Co/1.5Ce/1.5Zr/γ-$Al_2O_3$ catalyst demonstrated remarkable stability during a long reaction period of 70 h.

### Funding

The authors declare that no funds, grants, or other support were received during the preparation of this manuscript.

**Acknowledgments**

All authors contributed equally to this study. All authors prepared the manuscript.

**Data Availability**

The datasets generated during the current study are available from the corresponding author on reasonable request.

**Competing Interests**

The authors have no relevant financial or non-financial interests to disclose..

## References

[1] Y. Chen, L. Ma, R. Zhang, R. Ye, W. Liu, J. Wei, V. V. Ordomsky, and J. Liu, Carbon-supported Fe catalysts with well-defined active sites for highly selective alcohol production from Fischer-Tropsch synthesis, Applied Catalysis B: Environmental, vol. 312, p. 121393, 2022, doi: https://doi.org/10.1016/j.apcatb.2022.121393.

[2] R. Khalighi, F. Bahadoran, M. H. Panjeshahi, A. Zamaniyan, and N. Tahouni, Effects of Nickel Aluminate spinel ($NiAl_2O_4$) as catalyst support and promoters (Ru, Rh) in Fischer-Tropsch synthesis, Chemistry Select, vol. 5, no. 26, pp. 7934-7940, 2020, doi: https://doi.org/10.1002/slct.202000740.

[3] Z. Shariatinia., M. Abdollahi-Moghadam, DFT computations on surface physical adsorption of hydrocarbons produced in the Fischer-Tropsch synthesis on a CNT/Co nanocatalyst, Journal of Saudi Chemical Society, vol. 22, no. 7, pp. 786-808, 2018/11/01/ 2018, doi: https://doi.org/10.1016/j.jscs.2018.01.001.

[4] H.-j. Zhang, H.-f. Ma, H.-t. Zhang, W.-y. Ying, and D.-y. Fang, Effect of incorporation manner of Zr promoter on precipitated iron-based catalysts for Fischer-Tropsch synthesis, Journal of Coal Science and Engineering (China), vol. 18, no. 2, pp. 182-187, 2012, doi: https://doi.org/10.1007/s12404-012-0204-0.

[5] Z. Chen, Y. Meng, J. Lu, W. Zhou, Z. Yang, and A. Zhou, The effect of hydrophobically modified Iron catalysts with Hexadecyltrimethoxysilane on Fischer-Tropsch synthesis, Chemistry Select, vol. 8, no. 6, p. e202202903, 2023, doi: https://doi.org/10.1002/slct.202202903.

[6] K. T. Rommens, G. T. K. K. Gunasooriya, and M. Saeys, Key role of CO coverage for chain growth in Co-based Fischer–Tropsch synthesis, ACS Catalysis, vol. 14, no. 9, pp. 6696-6709, 2024/05/03 2024, doi: https://doi.org/10.1021/acscatal.3c04844.

[7] S. Guo, Q. Wang, M. Wang, Z. Ma, J. Wang, B. Hou, C. Chen, M. Xia, L. Jia, and D. Li, A comprehensive insight into the role of barium in catalytic performance of Co/$Al_2O_3$ catalyst for Fischer-Tropsch synthesis, Fuel, vol. 256, p. 115911, 2019, doi: https://doi.org/10.1016/j.fuel.2019.115911.

[8] A. N. Pour, S. M. K. Shahri, H. R. Bozorgzadeh, Y. Zamani, A. Tavasoli, and M. A. Marvast, Effect of Mg, La and Ca promoters on

the structure and catalytic behavior of iron-based catalysts in Fischer–Tropsch synthesis, Applied Catalysis A: General, vol. 348, no. 2, pp. 201-208, 2008, doi: https://doi.org/10.1016/j.apcata.2008.06.020.

[9] X. Zhao, S. Lv, L. Wang, L. Li, G. Wang, Y. Zhang, and J. Li, Comparison of preparation methods of iron-based catalysts for enhancing Fischer-Tropsch synthesis performance, Molecular Catalysis, vol. 449, pp. 99-105, 2018, doi: https://doi.org/10.1016/j.mcat.2018.02.010.

[10] S. Saheli, A. Reza Rezvani, A. Moghaddami, M. Dusek, and E. Samolova, Production of light olefins and $C_5$+ hydrocarbons in the Fischer-Tropsch synthesis by using inorganic precursor, Chemistry Select, vol. 7, no. 29, p. e202201286, 2022, doi: https://doi.org/10.1002/slct.202201286.

[11] T. Riedel, H. Schulz, G. Schaub, K.-W. Jun, J.-S. Hwang, and K.-W. Lee, Fischer–Tropsch on iron with $H_2$/CO and $H_2$/$CO_2$ as synthesis gases: the episodes of formation of the Fischer–Tropsch regime and construction of the catalyst, Topics in Catalysis, vol. 26, pp. 41-54, 2003, doi: https://doi.org/10.1023/B:TOCA.0000012986.46680.28

[12] D. Alihellal and L. Chibane, Comparative study of the performance of Fischer–Tropsch synthesis in conventional packed bed and in membrane reactor over Iron-and Cobalt-based catalysts, Arabian Journal for Science and Engineering, vol. 41, pp. 357-369, 2016, doi: https://doi.org/10.1007/s13369-015-1764-0

[13] D. Peña, L. Jensen, A. Cognigni, R. Myrstad, T. Neumayer, W. Van Beek, and M. Rønning, The effect of copper loading on Iron Carbide formation and surface species in Iron-Based Fischer–Tropsch synthesis catalysts, ChemCatChem, vol. 10, no. 6, pp. 1300-1312, 2018, doi: https://doi.org/10.1002/cctc.201701673.

[14] Z. Gholami, F. Gholami, Z. Tišler, J. Hubáček, M. Tomas, M. Bačiak, and M. Vakili, Production of light olefins via Fischer-Tropsch process using iron-based catalysts: A review, Catalysts, vol. 12, no. 2, p. 174, 2022, doi: https://doi.org/10.3390/catal12020174.

[15] J. Hong, W. Chu, P. A. Chernavskii, and A. Y. Khodakov, Effects of zirconia promotion on the structure and performance of smaller and larger pore silica-supported cobalt catalysts for Fischer–Tropsch synthesis, Applied Catalysis A: General, vol. 382, no. 1, pp. 28-35, 2010, doi: https://doi.org/10.1016/j.apcata.2010.04.020.

[16] M. Martinelli, M. Mehrbod, C. Dawson, B. H. Davis, L. Lietti, D. C. Cronauer, A. J. Kropf, C. L. Marshall, and G. Jacobs, Fischer-Tropsch synthesis: Foregoing calcination and utilizing reduction promoters leads to improved conversion and selectivity with Co/silica, Applied Catalysis A: General, vol. 559, pp. 153-166, 2018, doi: https://doi.org/10.1016/j.apcata.2018.04.010.

[17] T. Lin, K. Gong, C. Wang, Y. An, X. Wang, X. Qi, S. Li, Y. Lu, L. Zhong, and Y. Sun, Fischer–Tropsch Synthesis to Olefins: Catalytic performance and structure evolution of $Co_2C$-Based catalysts under a $CO_2$ environment, ACS Catalysis, vol. 9, no. 10, pp. 9554-9567, 2019/10/04 2019, doi: https://doi.org/10.1021/acscatal.9b02513.

[18] S. Wang, Q. Yin, J. Guo, B. Ru, and L. Zhu, Improved Fischer–Tropsch synthesis for gasoline over Ru, Ni promoted Co/HZSM-5 catalysts, Fuel, vol. 108, pp. 597-603, 2013/06/01/ 2013, doi: https://doi.org/10.1016/j.fuel.2013.02.021.

[19] A. Wang, M. Luo, B. Lü, Y. Song, M. Li, and Z. Yang, Effect of Na, Cu and Ru on metal-organic framework-derived porous carbon supported iron catalyst for Fischer-Tropsch synthesis, Molecular Catalysis, vol. 509, p. 111601, 2021, doi: https://doi.org/10.1016/j.mcat.2021.111601.

[20] K. Mazurova, A. Miyassarova, O. Eliseev, R. Yakovenko, R. Kazantsev, A. Glotov, and A. Stavitskaya, Fischer–Tropsch synthesis over RuCo catalysts: An effect of ligands on the active phase properties and catalytic activity, Chemical Engineering Journal, vol. 488, p. 150837, 2024/05/15/ 2024, doi: https://doi.org/10.1016/j.cej.2024.150837.

[21] M. Rezaei Kafrani, A. A. Beni, and Z. P. Nodeh, Preparation of cobalt-ruthenium nanocatalysts supported on nitrogen-doped graphene aerogel and carbon nanotubes in Fischer-Tropsch synthesis, Arabian Journal of Chemistry, vol. 16, no. 8, p. 104914, 2023, doi: https://doi.org/10.1016/j.arabjc.2023.104914.

[22] P. Hunpinyo, P. Narataruksa, S. Tungkamani, K. Pana-Suppamassadu, N. Chollacoop, H. Sukkathanyawat, and P. Jiamrittiwong, A comprehensive small and pilot-scale fixed-bed reactor approach for testing Fischer–Tropsch catalyst activity and performance on a BTL route, Arabian Journal of Chemistry, vol. 10, pp. S2806-S2828, 2017/05/01/ 2017, doi: https://doi.org/10.1016/j.arabjc.2013.11.004.

[23] W. Zhao, Y. Wang, Z. Li, H. Wang, J. Wu, J. Huang, and Y. Zhao, The influence of hierarchical zeolite composition and pore structure on behavior of cobalt-based Fischer–Tropsch synthesis catalysts, Journal of Porous Materials, vol. 22, pp. 1097-1104, 2015, doi: https://doi.org/10.1007/s10934-015-9984-y.

[24] M. Safari, A. Haghtalab, and F. A. Roghabadi, Tuning the strong metal support interaction of the Fischer-Tropsch synthesis silica-coated cobalt-based nano-catalyst, International Journal of Hydrogen Energy, vol. 65, pp. 348-361, 2024/05/02/ 2024, doi: https://doi.org/10.1016/j.ijhydene.2024.03.345.

[25] F. Haghighi, A. Ahmadpour, and A. Nakhaei Pour, Fischer-Tropsch synthesis by a Cobalt-based Carbon aerogel catalyst, Chemical Engineering & Technology, vol. 47, no. 2, pp. 297-307, 2024, doi: https://doi.org/10.1002/ceat.202300325.

[26] S. Saheli, A. R. Rezvani, A. Izadpanah, M. Dusek, and V. Eigner, Design novel inorganic precursors for producing clean fuels by using Fischer-Tropsch synthesis, Journal of Saudi Chemical Society, vol. 23, no. 8, pp. 1070-1079, 2019, doi: https://doi.org/10.1016/j.jscs.2019.06.003.

[27] S. Alinia, M. Masoumi, A. Haghtalab, M. Otadi, and F. Yaripour, Enhanced Fischer-Tropsch synthesis performance using graphene Nanosheets-supported Cobalt-Ruthenium Nanocatalysts: Comparative study with γ-Alumina and carbon nanotubes supports, Arabian Journal of Chemistry, vol. 17, no. 2, p. 105503, 2024, doi: https://doi.org/10.1016/j.arabjc.2023.105503.

[28] Y. Liu, B. de Tymowski, F. Vigneron, I. Florea, O. Ersen, C. Meny, P. Nguyen, C. Pham, F. Luck, and C. Pham-Huu, Titania-decorated Silicon Carbide-containing Cobalt catalyst for Fischer–Tropsch synthesis, ACS Catalysis, vol. 3, no. 3, pp. 393-404, 2013/03/01 2013, doi: https://doi.org/10.1021/cs300729p.

[29] X. Wang, C. Zhang, Q. Chang, L. Wang, B. Lv, J. Xu, H. Xiang, Y. Yang, and Y. Li, Enhanced Fischer-Tropsch synthesis performances of Fe/h-BN catalysts by Cu and Mn, Catalysis Today, vol. 343, pp. 91-100, 2020, doi: https://doi.org/10.1016/j.cattod.2019.01.009.

[30] N. Luo, W. Yang, L. Feng, S. Huang, P. Huang, and M. Wei, Recent advances in utilizing molybdenum and tungsten carbides for fischer-tropsch synthesis, Molecular Catalysis, vol. 553, p. 113683, 2024/01/15/ 2024, doi: https://doi.org/10.1016/j.mcat.2023.113683.

[31] A. Eshraghi, A. A. Mirzaei, R. Rahimi, and H. Atashi, Fischer-Tropsch Synthesis on Fe-Co-Pt/γ-$Al_2O_3$ catalyst: A mass transfer, kinetic and mechanistic study, Korean Journal of Chemical

Engineering, vol. 37, pp. 1699-1708, 2020, doi: https://doi.org/10.1007/s11814-020-0590-6.

[32] Y. Zhang, G. Jacobs, D. E. Sparks, M. E. Dry, and B. H. Davis, CO and $CO_2$ hydrogenation study on supported cobalt Fischer–Tropsch synthesis catalysts, Catalysis Today, vol. 71, no. 3-4, pp. 411-418, 2002, doi: https://doi.org/10.1016/S0920-5861(01)00468-0.

[33] S. Zhao, W. Cai, Y. Li, H. Yu, S. Zhang, and L. Cui, Syngas production from ethanol dry reforming over $Rh/CeO_2$ catalyst, Journal of Saudi Chemical Society, vol. 22, no. 1, pp. 58-65, 2018/01/01/ 2018, doi: https://doi.org/10.1016/j.jscs.2017.07.003.

[34] A. Y. Khodakov, R. Bechara, and A. Griboval-Constant, Fischer–Tropsch synthesis over silica supported cobalt catalysts: mesoporous structure versus cobalt surface density, Applied Catalysis A: General, vol. 254, no. 2, pp. 273-288, 2003, doi: https://doi.org/10.1016/S0926-860X(03)00489-7.

[35] S. Hosseini, A. Taeb, F. Feyzi, and F. Yaripour, Fischer–Tropsch synthesis over Ru promoted $Co/\gamma$-$Al_2O_3$ catalysts in a CSTR, Catalysis communications, vol. 5, no. 3, pp. 137-143, 2004, doi: https://doi.org/10.1016/j.catcom.2003.11.013.

[36] G. Jacobs, J. A. Chaney, P. M. Patterson, T. K. Das, and B. H. Davis, Fischer–Tropsch synthesis: study of the promotion of Re on the reduction property of $Co/Al_2O_3$ catalysts by in situ EXAFS/XANES of Co K and Re LIII edges and XPS, Applied Catalysis A: General, vol. 264, no. 2, pp. 203-212, 2004, doi: https://doi.org/10.1016/j.apcata.2003.12.049.

[37] T. K. Das, G. Jacobs, P. M. Patterson, W. A. Conner, J. Li, and B. H. Davis, Fischer–Tropsch synthesis: characterization and catalytic properties of rhenium promoted cobalt alumina catalysts, Fuel, vol. 82, no. 7, pp. 805-815, 2003, doi: https://doi.org/10.1016/S0016-2361(02)00361-7.

[38] X. Huang and C. B. Roberts, Selective Fischer–Tropsch synthesis over an $Al_2O_3$ supported cobalt catalyst in supercritical hexane, Fuel Processing Technology, vol. 83, no. 1-3, pp. 81-99, 2003, doi: https://doi.org/10.1016/S0378-3820(03)00060-2.

[39] J. Horáček, Fischer–Tropsch synthesis, the effect of promoters, catalyst support, and reaction conditions selection, Monatshefte für Chemie - Chemical Monthly, vol. 151, no. 5, pp. 649-675, 2020/05/01 2020, doi: https://doi.org/10.1007/s00706-020-02590-w.

[40] L. Guczi, G. Stefler, O. Geszti, Z. Koppány, Z. Kónya, É. Molnár, M. Urbán, and I. Kiricsi, CO hydrogenation over cobalt and iron catalysts supported over multiwall carbon nanotubes: effect of preparation, Journal of Catalysis, vol. 244, no. 1, pp. 24-32, 2006, doi: https://doi.org/10.1016/j.jcat.2006.08.012.

[41] D. Schanke, S. Eri, E. Rytter, C. Aaserud, A.-M. Hilmen, O. A. Lindvg, E. Bergene, and A. Holmen, Fischer-Tropsch synthesis on cobalt catalysts supported on different aluminas, Studies in surface science and catalysis, vol. 147, pp. 301-306, 2004, doi: https://doi.org/10.1016/S0167-2991(04)80068-5.

[42] S. Storsæter, Ø. Borg, E. A. Blekkan, and A. Holmen, Study of the effect of water on Fischer–Tropsch synthesis over supported cobalt catalysts, Journal of Catalysis, vol. 231, no. 2, pp. 405-419, 2005, doi: https://doi.org/10.1016/j.jcat.2005.01.036.

[43] Q. Cheng, Y. Liu, S. Lyu, Y. Tian, Q. Ma, and X. Li, Manipulating metal-support interactions of metal catalysts for Fischer-Tropsch synthesis, Chinese Journal of Chemical Engineering, vol. 35, pp. 220-230, 2021, doi: https://doi.org/10.1016/j.cjche.2021.05.013.

[44] J. Gaube and H.-F. Klein, The promoter effect of alkali in Fischer-Tropsch iron and cobalt catalysts, Applied Catalysis A: General, vol. 350, no. 1, pp. 126-132, 2008, doi: https://doi.org/10.1016/j.apcata.2008.08.007.

[45] Ø. Borg, P. Dietzel, A. Spjelkavik, E. Tveten, J. Walmsley, S. Diplas, S. Eri, A. Holmen, and E. Rytter, Fischer–Tropsch synthesis: Cobalt particle size and support effects on intrinsic activity and product distribution, Journal of Catalysis, vol. 259, no. 2, pp. 161-164, 2008, doi: https://doi.org/10.1016/j.jcat.2008.08.017.

[46] R. Guettel and T. Turek, Comparison of different reactor types for low temperature Fischer–Tropsch synthesis: A simulation study, Chem. Eng. Sci., vol. 64, no. 5, pp. 955-964, 2009, doi: https://doi.org/10.1016/j.ces.2008.10.059.

[47] H. Janani, A. R. Rezvani, G. H. Grivani, and A. A. Mirzaei, Fischer–Tropsch synthesis of hydrocarbons over new Co/Ce bimetallic catalysts derived from Dipicolinate and carbonyl metal complexes, Journal of Inorganic and Organometallic Polymers and Materials, vol. 25, pp. 1169-1182, 2015, doi: https://doi.org/10.1007/s10904-015-0225-2.

[48] G. Jacobs, M. C. Ribeiro, W. Ma, Y. Ji, S. Khalid, P. T. Sumodjo, and B. H. Davis, Group 11 (Cu, Ag, Au) promotion of 15% $Co/Al_2O_3$ Fischer–Tropsch synthesis catalysts, Applied Catalysis A: General, vol. 361, no. 1-2, pp. 137-151, 2009, doi: https://doi.org/10.1016/j.apcata.2009.04.007.

[49] J. Li, X. Cheng, C. Zhang, Q. Chang, J. Wang, X. Wang, Z. Lv, W. Dong, Y. Yang, and Y. Li, Effect of alkalis on iron-based Fischer-Tropsch synthesis catalysts: Alkali-$FeO_x$ interaction, reduction, and catalytic performance, Applied Catalysis A: General, vol. 528, pp. 131-141, 2016/11/25/ 2016, doi: https://doi.org/10.1016/j.apcata.2016.10.006.

[50] B. Gu, V. V. Ordomsky, M. Bahri, O. Ersen, P. A. Chernavskii, D. Filimonov, and A. Y. Khodakov, Effects of the promotion with bismuth and lead on direct synthesis of light olefins from syngas over carbon nanotube supported iron catalysts, Applied Catalysis B: Environmental, vol. 234, pp. 153-166, 2018/10/15/ 2018, doi: https://doi.org/10.1016/j.apcatb.2018.04.025.

[51] A. A. Ayandiran, P. E. Boahene, S. Nanda, A. K. Dalai, and Y. Hu, Hydroprocessing of oleic acid for the production of aviation turbine fuel range hydrocarbons over bimetallic Fe-Cu/$SiO_2$-$Al_2O_3$ catalysts promoted by Sn, Ti and Zr, Molecular Catalysis, vol. 523, p. 111358, 2022/05/01/ 2022, doi: https://doi.org/10.1016/j.mcat.2020.111358.

[52] A. Y. Khodakov, Fischer-Tropsch synthesis: Relations between structure of cobalt catalysts and their catalytic performance, Catalysis Today, vol. 144, no. 3-4, pp. 251-257, 2009, doi: https://doi.org/10.1016/j.cattod.2008.10.036.

[53] Z. Pan and D. B. Bukur, Fischer–Tropsch synthesis on Co/ZnO catalyst—Effect of pretreatment procedure, Applied Catalysis A: General, vol. 404, no. 1, pp. 74-80, 2011/09/19/ 2011, doi: https://doi.org/10.1016/j.apcata.2011.07.012.

[54] A. Saib, D. Moodley, I. Ciobîcă, M. Hauman, B. Sigwebela, C. Weststrate, J. Niemantsverdriet, and J. Van de Loosdrecht, Fundamental understanding of deactivation and regeneration of cobalt Fischer–Tropsch synthesis catalysts, Catalysis Today, vol. 154, no. 3-4, pp. 271-282, 2010, doi: https://doi.org/10.1016/j.cattod.2010.02.008.

[55] B. Todic, M. Mandic, N. Nikacevic, and D. B. Bukur, Effects of process and design parameters on heat management in fixed bed Fischer-Tropsch synthesis reactor, Korean Journal of Chemical

Engineering, vol. 35, pp. 875-889, 2018, doi: https://doi.org/10.1007/s11814-017-0335-3.

[56] N. C. Milani, Y. Zamani, S. Baniyaghoob, and A. N. Pour, Synergistic effect of Zr and K promoters on iron-based catalysts in CO hydrogenation reaction, Journal of Saudi Chemical Society, p. 101850, 2024, doi: https://doi.org/10.1016/j.jscs.2024.101850.

[57] B. Moshtari, S. H. Hashemabadi, and Y. Zamani, The effect of Cobalt to Iron ratio on novel Perovskite catalysts for Fischer-Tropsch synthesis, Journal of Petroleum Science and Technology, vol. 13, no. 2, pp. 20-28, 2023, doi: https://doi.org/10.22078/jpst.2023.5251.1904.

[58] V. Garcilaso, J. Barrientos, L. Bobadilla, O. Laguna, M. Boutonnet, M. Centeno, and J. Odriozola, Promoting effect of $CeO_2$, $ZrO_2$ and Ce/Zr mixed oxides on Co/γ-$Al_2O_3$ catalyst for Fischer-Tropsch synthesis, Renewable energy, vol. 132, pp. 1141-1150, 2019, doi: https://doi.org/10.1016/j.renene.2018.08.080.

[59] F. Pardo-Tarifa, S. Cabrera, M. Sanchez-Dominguez, and M. Boutonnet, Ce-promoted Co/$Al_2O_3$ catalysts for Fischer–Tropsch synthesis, International journal of hydrogen energy, vol. 42, no. 15, pp. 9754-9765, 2017, doi: https://doi.org/10.1016/j.ijhydene.2017.01.056.

[60] X. Zhang, H. Su, Y. Zhang, and X. Gu, Effect of $CeO_2$ promotion on the catalytic performance of Co/$ZrO_2$ catalysts for Fischer–Tropsch synthesis, Fuel, vol. 184, pp. 162-168, 2016, doi: https://doi.org/10.1016/j.fuel.2016.06.125.

[61] C. Wang, J. Zhang, and J. Chen, Preparation of single-phase Iron Nitrides and investigation of their Fischer-Tropsch synthesis performance, Chemistry Select, vol. 5, no. 13, pp. 3953-3958, 2020, doi: https://doi.org/10.1002/slct.202000456.

[62] M. Dowlati, N. Siyavashi, and H. R. Azizi, Sintering and coking: Effect of preparation methods on the deactivation of Co–Ni/$TiO_2$ in Fischer–Tropsch synthesis, Arabian Journal for Science and Engineering, vol. 43, pp. 2441-2450, 2018, doi: https://doi.org/10.1007/s13369-017-2845-z.

[63] Z. Han, W. Qian, H. Ma, X. Wu, H. Zhang, Q. Sun, and W. Ying, Study of the Fischer–Tropsch synthesis on nano-precipitated iron-based catalysts with different particle sizes, RSC advances, vol. 10, no. 70, pp. 42903-42911, 2020, doi: https://doi.org/10.1039/D0RA08469G.

[64] L. Niu, X. Liu, X. Wen, Y. Yang, J. Xu, and Y. Li, Effect of potassium promoter on phase transformation during $H_2$ pretreatment of a $Fe_2O_3$ Fischer Tropsch synthesis catalyst precursor, Catalysis Today, vol. 343, pp. 101-111, 2020, doi: https://doi.org/10.1016/j.cattod.2019.01.054.

[65] L. Guczi, Z. Schay, G. Stefler, and F. Mizukami, Bimetallic catalysis: CO hydrogenation over palladium–cobalt catalysts prepared by sol/gel method, Journal of Molecular Catalysis A: Chemical, vol. 141, no. 1-3, pp. 177-185, 1999, doi: https://doi.org/10.1016/S1381-1169(98)00261-1.

[66] H. Xiong, Y. Zhang, K. Liew, and J. Li, Catalytic performance of zirconium-modified Co/$Al_2O_3$ for Fischer–Tropsch synthesis, Journal of Molecular Catalysis A: Chemical, vol. 231, no. 1-2, pp. 145-151, 2005, doi: https://doi.org/10.1016/j.molcata.2004.12.033.

[67] Z. Gholami, Z. Tišler, and V. Rubáš, Recent advances in Fischer-Tropsch synthesis using cobalt-based catalysts: A review on supports, promoters, and reactors, Catalysis Reviews, vol. 63, no. 3, pp. 512-595, 2021, doi: https://doi.org/10.1080/01614940.2020.1762367.

[68] Y. Wu, W. Zhang, M. Yang, Y. Zhao, Z. Liu, and J. Yan, Cobalt supported on Zr-modified $SiO_2$ as an efficient catalyst for Fischer–Tropsch synthesis, RSC advances, vol. 7, no. 39, pp. 24157-24162, 2017, doi: https://doi.org/10.1039/C7RA01756A.

[69] A. L. Khalaf, F. K. Al-Zuhairi, W. A. Kadhim, and M. H. Ab Rahim, The effects of cerium promoter on the performance of cobalt-based catalysts in fischer tropsch synthesis for liquid fuel production, IIUM Engineering Journal, vol. 21, no. 2, pp. 1-11, 2020, doi: https://doi.org/10.31436/iiumej.v21i2.1150.

[70] M. Arsalanfar, A. Mirzaei, H. Bozorgzadeh, H. Atashi, S. Shahriari, and A. Pourdolat, Structural characteristics of supported cobalt–cerium oxide catalysts used in Fischer–Tropsch synthesis, Journal of Natural Gas Science and Engineering, vol. 9, pp. 119-129, 2012, doi: https://doi.org/10.1016/j.jngse.2012.05.015.

[71] E. Rytter, N. E. Tsakoumis, and A. Holmen, On the selectivity to higher hydrocarbons in Co-based Fischer–Tropsch synthesis, Catalysis Today, vol. 261, pp. 3-16, 2016, doi: https://doi.org/10.1016/j.cattod.2015.09.020.

[72] M. Mehrbod, M. Martinelli, A. G. Martino, D. C. Cronauer, A. J. Kropf, C. L. Marshall, and G. Jacobs, Fischer-Tropsch synthesis: Direct cobalt nitrate reduction of promoted Co/$TiO_2$ catalysts, Fuel, vol. 245, pp. 488-504, 2019, doi: https://doi.org/10.1016/j.fuel.2019.02.083